Benchmarking Burst Super-Resolution for Polarization Images: Noise Dataset and Analysis

Inseung Hwang Kiseok Choi Hyunho Ha Min H. Kim
KAIST
{ishwang; kschoi; hhha; minhkim}@vclab.kaist.ac.kr

Abstract

Snapshot polarization imaging calculates polarization states from linearly polarized subimages. To achieve this, a polarization camera employs a double Bayer-patterned sensor to capture both color and polarization. It demonstrates low light efficiency and low spatial resolution, resulting in increased noise and compromised polarization measurements. Although burst super-resolution effectively reduces noise and enhances spatial resolution, applying it to polarization imaging poses challenges due to the lack of tailored datasets and reliable ground truth noise statistics. To address these issues, we introduce PolarNS and PolarBurstSR, two innovative datasets developed specifically for polarization imaging. PolarNS provides characterization of polarization noise statistics, facilitating thorough analysis, while PolarBurstSR functions as a benchmark for burst super-resolution in polarization images. These datasets, collected under various real-world conditions, enable comprehensive evaluation. Additionally, we present a model for analyzing polarization noise to quantify noise propagation, tested on a large dataset captured in a darkroom environment. As part of our application, we compare the latest burst super-resolution models, highlighting the advantages of training tailored to polarization compared to RGB-based methods. This work establishes a benchmark for polarization burst super-resolution and offers critical insights into noise propagation, thereby enhancing polarization image reconstruction. Both code and dataset are publicly available on https://github.com/KAIST-VCLAB/polarns.

1. Introduction

Polarization imaging provides valuable scene information by capturing the polarization state of light, which changes upon interaction with surfaces according to the Fresnel equations [1]. This property enables polarization imaging to trace light sources and infer surface characteristics, making it widely applicable in areas, such as dehazing [20, 46, 61, 74], transparent object segmentation [36, 50, 54], enhancement of ToF imaging [4, 5, 33, 62], reflection removal [38, 41, 48, 70], specular-diffuse separation [24, 49, 57], facial acquisition [2, 25, 27, 30, 58], shape-from-polarization techniques [1, 31, 51], RGB-D integration [35], normal regularization [64, 67], multiview acquisition [12, 13, 73, 75], deep learning approaches [3, 15–17, 22, 42], and neural implicit representations [43, 72]. However, polarization-based measurements are highly susceptible to noise, which significantly affects their accuracy and reliability. Unlike standard intensity images, polarization properties are not captured directly but are instead derived from multiple intensity measurements through

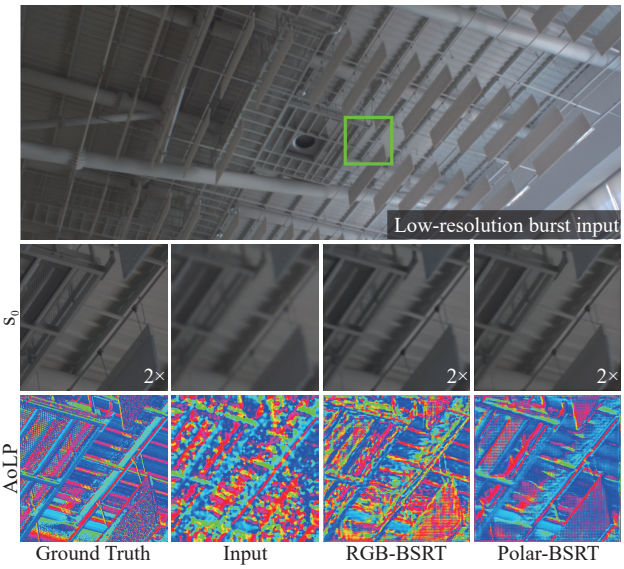

Figure 1. The top row displays the low-resolution burst input captured using a polarization camera. The second row presents close-up comparisons of different methods: GT, the low-resolution input, the 2× super-resolution results of the RGB-trained BSRT [47] trained on a conventional RGB dataset, and the Polar-BSRT method trained on our polarization image dataset. Training with our dedicated polarization dataset significantly improves both the spatial resolution of the intensity image (s_0) and the angle of linear polarization (AoLP) map, demonstrating the importance of polarization-specific training for burst super-resolution.

computational models. This process inherently amplifies noise, making polarization-sensitive analysis particularly challenging.

The propagation of noise in polarization calculations is complex, often requiring approximations such as first-order Taylor expansions [6, 11, 14, 29, 44, 59] or assumptions that noise follows an additive white Gaussian distribution in the Stokes vector components [39, 53, 56, 63]. The lack of precise noise characterization limits the development of robust denoising methods. Moreover, modern snapshot polarization cameras employ a double Bayer-patterned sensor to capture both color and polarization information, resulting in lower light efficiency and reduced spatial resolution. These factors collectively lead to increased noise, further degrading polarization-based analysis.

While conventional burst super-resolution (BSR) techniques have successfully mitigated noise and enhanced resolution in standard intensity images, their application to polarization imaging remains unexplored because there are no dedicated training datasets available. Without reliable polarization burst super-resolution datasets or detailed noise statistics, it is impossible to train or evaluate polarization-aware super-resolution models effectively.

To address these challenges, we introduce two novel datasets specifically designed for polarization imaging: PolarNS and PolarBurstSR. PolarNS is the first large-scale dataset focused on polarization noise statistics, providing a detailed characterization of noise propagation in polarization images. Captured under diverse real-world conditions with high precision, it serves as a benchmark for analyzing polarization noise and evaluating denoising techniques. To complement this dataset, we propose a polarization noise analysis model that quantifies noise propagation through an analytical approach with minimal assumptions, based on a shot and read noise model of polarization sensors. This model estimates the statistical distribution of polarization properties in the presence of noise, offering a physically grounded validation of the dataset.

In addition, we establish PolarBurstSR, a dataset designed for training and evaluating burst super-resolution (BSR) models in polarization imaging. By providing high-quality image sequences tailored to polarization data, PolarBurstSR enables the development of BSR techniques that effectively enhance spatial resolution and reduce noise. See Figure 1 for an example. To promote further research, we will publicly release our datasets, along with pretrained models and training pipelines for burst super-resolution on polarization images.

2. Related Work

Noise Analysis for Polarization Imaging. Traditional noise analysis in polarization imaging has focused on controlled ellipsometric setups with strong polarization signals, multiple image captures, and polarized lighting [23, 26, 28, 52, 60, 65]. Recent work has extended to noise propagation analysis in polarization properties such as the degree of linear polarization (DoLP) and angle of linear polarization (AoLP), often using first-order Taylor expansions [6, 11, 14, 29, 44, 59]. However, these methods assume high signal-to-noise ratios and do not generalize well to real-world vision tasks where polarization signals are weak and noise dominates. Unlike previous approaches, our work introduces a snapshot polarization imaging noise model tailored for four-channel linear polarization cameras in uncontrolled settings. By directly modeling noise propagation with minimal assumptions, our method provides a more comprehensive characterization, capturing not just variance but the full distribution and bias of polarization properties.

Polarization Image Datasets. Polarization datasets have been developed for high-level vision tasks such as segmentation, geometry estimation, and reflection removal [3, 15, 34, 41, 42, 45, 50, 66], typically using off-the-shelf polarization cameras. Low-level tasks, such as demosaicing and sparse filter design, require full-frame polarization data captured using rotating polarizers [40, 55], though these setups are impractical for hand-held capture. In contrast, we introduce a new polarization image dataset specifically designed for burst super-resolution and noise analysis. Our dataset provides both image variance and metadata, making it uniquely suited for denoising and super-resolution tasks. To ensure high-quality ground truth, we employ a burst shot method, offering 14 low-resolution burst images per scene alongside a high-resolution and noise suppressed reference. This dataset serves as a benchmark for polarization burst super-resolution, addressing a critical gap in existing resources.

Polarization Imaging Applications. Polarization imaging is widely used in applications such as dehazing [20, 46, 61, 74], reflection removal [38, 41, 48, 70], transparent object segmentation [36, 50, 54], and ToF imaging enhancement [4, 5, 33, 62]. While specular reflection provides strong polarization signals, diffuse polarization is weak and directly affected by noise, making applications like shape-from-polarization [1, 31, 51] highly sensitive to noise. Our work introduces a dedicated noise model for DoLP and AoLP, addressing the lack of systematic noise characterization in diffuse polarization imaging. Additionally, our dataset includes real-world scenes such as glass-through, reflection-dominant, and road surface imaging, where burst super-resolution significantly reduces noise.

Multi-Frame Super-Resolution. Multi-frame super-resolution (SR) has evolved from early algorithmic approaches [19, 21, 32, 68] to modern burst super-resolution (BSR) methods that leverage hand-held motion [71]. Learning-based BSR was first introduced by Bhat et al. [7],

whose dataset and evaluation metrics have been widely adopted [8, 9, 18, 37, 47, 69]. Recent expansions include self-supervised learning and datasets with improved scene variety [9, 69]. However, burst super-resolution has not been explored for polarization imaging, where noise characteristics differ significantly from RGB images. We introduce PolarBurstSR, the first burst super-resolution dataset and benchmarking framework for polarization imaging, enabling denoising and high-resolution reconstruction in this domain.

3. Dataset

3.1. Polarization Noise Statistic Dataset

We introduce the noise-reduced image and the noise statistic dataset, called PolarNS. We capture this data using an off-the-shelf polarization RGB camera (FLIR BFS-U3-51S5PC-C) and a 35mm lens. The noise statistics of each scene are calculated from the burst images taken in a fixed position, ensuring that all our scenes remain static. Our scenes consist of 54 objects in a darkroom and 190 indoor and outdoor scenes. We capture 10,000 images for each object in the darkroom and around 1,000 images for each indoor and outdoor scene. The illumination also remains static throughout the capture period. The exposure time is set as a multiple of the AC current period for the indoor scenes. For the outdoor scenes, occlusion caused by clouds leads to variations in capture time, so we capture the scenes when there are no clouds in the sky or at nighttime. We calculate the mean and variance per pixel from the raw burst images. The dataset includes the mean and variance of the scenes, along with metadata (e.g., exposure time, gain) for the images. Figure 2 shows examples of our datasets.

3.2. Burst Super-Resolution Dataset

We also acquire a polarization burst super-resolution dataset called PolarBurstSR. We follow the same process as the BurstSR dataset [7] using a polarization camera. The ground truth of the burst dataset is derived from the mean image of the noise statistic dataset. When the noise statistics are captured, 14 hand-held burst images are taken simultaneously. The total number of images is 160, distributed among the training, validation, and test sets as 112, 16, and 32 respectively. Refer to the supplemental document for the super-resolution image processing details.

4. Noise analysis model

We derive a new noise model for the Stokes vector and its polarization properties, specifically designed for a conventional image denoising and super-resolution framework. Key physical findings from this noise model include:

- The variance of the Stokes vector components depends linearly on the s_0 component of the Stokes vector.

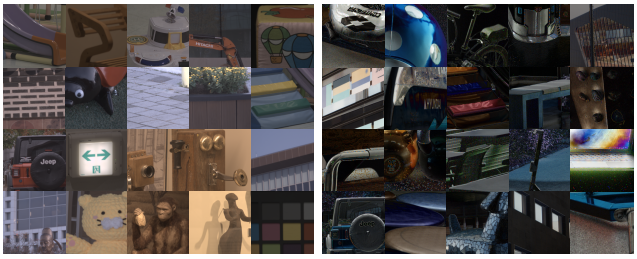

Figure 2. Our dataset examples presented in color intensity images s_0 (left) and their DoLP properties (right).

- The degree of linear polarization follows a Rician distribution influenced by the intensity of the s_0 component, polarization intensity, and Stokes vector noise.
- The angle of linear polarization exhibits a Gaussian-like distribution shaped by the ratio of polarization intensity to Stokes vector noise.

In the following subsections, we will demonstrate each of these properties in detail.

4.1. Background

The light is an electromagnetic wave in which the electric field oscillates perpendicularly to the direction of wave propagation. This perpendicular oscillation allows for a degree of freedom in the oscillation, which gives light its orientation called polarization. The electric field can oscillate linearly, circularly, or elliptically, depending on the orientation and the retardation of the perpendicular components. The Stokes vector $\mathbf{s} = \begin{bmatrix} s_0 & s_1 & s_2 & s_3 \end{bmatrix}^T$ is the four-dimensional vector, which represents the polarization state of light. s_0 indicates the total intensity of light, while s_1, s_2, and s_3 refer to the intensities of the polarized components, describing horizontal/vertical, diagonal/antidiagonal, and circular polarization, respectively. In this paper, we focus solely on linearly polarized light because the employed polarization camera can capture linear polarization only; therefore, we do not utilize s_3 and represent the Stokes vector as a three-dimensional vector.

From polarization, we can obtain useful properties: the degree of linear polarization and the angle of linear polarization. These properties provide intuitive information about polarization. DoLP is the ratio of the intensity of linear polarization to the total intensity. DoLP, denoted as ψ, is defined as: $\psi = \frac{s_{pol}}{s_0} = \frac{\sqrt{s_1^2+s_2^2}}{s_0}$, where s_{pol} represents the intensity of the polarized components, indicating the degree of light polarization.

The AoLP refers to the orientation of linear polarization. The AoLP, denoted as ϕ, is defined as: $\phi = \frac{1}{2}\tan^{-1}(\frac{s_2}{s_1})$. It indicates the orientation of the surface normal during diffuse reflection.

To acquire the linear components of the Stokes vector, at least three different angle linear polarization images are required. An off-the-shelf polarization camera uses four an-

gles of linear polarization, specifically 0, 45, 90, and 135 degrees, and we will derive the equations in the case of these four angles in this paper. The polarization images $I_{(\cdot)}$ can be expressed as

$$\begin{bmatrix} I_0 \\ I_{45} \\ I_{90} \\ I_{135} \end{bmatrix} = \frac{1}{2} \begin{bmatrix} 1 & 1 & 0 \\ 1 & 0 & 1 \\ 1 & -1 & 0 \\ 1 & 0 & -1 \end{bmatrix} \begin{bmatrix} s_0 \\ s_1 \\ s_2 \end{bmatrix}. \tag{1}$$

The reconstructed Stokes vector $\hat{\mathbf{s}}$ is expressed as

$$\hat{\mathbf{s}} = \begin{bmatrix} \frac{1}{2}\left(\hat{I}_0 + \hat{I}_{45} + \hat{I}_{90} + \hat{I}_{135}\right) \\ \hat{I}_0 - \hat{I}_{90} \\ \hat{I}_{45} - \hat{I}_{135} \end{bmatrix}, \tag{2}$$

from observed images $\hat{I}_{(\cdot)}$.

4.2. Stokes vector noise model

Image noise has two major categories: shot noise and read noise. Shot noise arises from the quantum properties of light. It follows a Poisson distribution regarding the number of photons and can be approximated by a Gaussian distribution. Read noise consists of residual noise sources, such as thermal noise, source follower noise, and ADC quantization noise. In many applications, read noise is modeled as zero-mean Gaussian noise. The observed image $\hat{I}$ can be modeled as the random variable:

$$\hat{I} \sim \mathcal{N}\left(I, I\sigma_s^2 + \sigma_r^2\right), \tag{3}$$

where σ_s is the coefficient of shot noise, and σ_r is the standard deviation of read noise.

Equations (1) and (3) express the linear polarization image noise model as

$$\begin{aligned} \hat{I}_0 &\sim \mathcal{N}\left(\tfrac{1}{2}s_0 + \tfrac{1}{2}s_1, \left(\tfrac{1}{2}s_0 + \tfrac{1}{2}s_1\right)\sigma_s^2 + \sigma_r^2\right), \\ \hat{I}_{45} &\sim \mathcal{N}\left(\tfrac{1}{2}s_0 + \tfrac{1}{2}s_2, \left(\tfrac{1}{2}s_0 + \tfrac{1}{2}s_2\right)\sigma_s^2 + \sigma_r^2\right), \\ \hat{I}_{90} &\sim \mathcal{N}\left(\tfrac{1}{2}s_0 - \tfrac{1}{2}s_1, \left(\tfrac{1}{2}s_0 - \tfrac{1}{2}s_1\right)\sigma_s^2 + \sigma_r^2\right), \text{and} \\ \hat{I}_{135} &\sim \mathcal{N}\left(\tfrac{1}{2}s_0 - \tfrac{1}{2}s_2, \left(\tfrac{1}{2}s_0 - \tfrac{1}{2}s_2\right)\sigma_s^2 + \sigma_r^2\right). \end{aligned} \tag{4}$$

Each image is an independent random variable. The random variables are independent and normally distributed, so they can be subjected to arithmetic operations. By Equations (2) and (4), the Stokes vector model is expressed as

$$\hat{s}_0 \sim \mathcal{N}\left(s_0, \tfrac{1}{2}\sigma_v^2\right), \;\; \hat{s}_1 \sim \mathcal{N}\left(s_1, \sigma_v^2\right), \;\; \hat{s}_2 \sim \mathcal{N}\left(s_2, \sigma_v^2\right), \tag{5}$$

where Stokes vector noise $\sigma_v^2 = s_0\sigma_s^2 + 2\sigma_r^2$.

Note that $\hat{s}_0$ depends on $\hat{s}_1$ and $\hat{s}_2$, while $\hat{s}_1$ and $\hat{s}_2$ are independent of one another. The following sections are based on this independence, which exists only in the case of the four angles.

4.3. DoLP noise model

DoLP is the ratio of the polarization components to the total intensity. The distributions of DoLP and AoLP, when the polarization component follows a Gaussian distribution, are known from previous astronomical studies [56, 63]. Intuitively, the distribution of the DoLP represents the marginal distribution of the radius of the noncentral Gaussian distribution, which corresponds to the line integral along the blue circle in Figure 3(a).

The division of the random variables makes it difficult to derive the equations. Because the noise of total intensity is much smaller than the total intensity, we approximate the observed total intensity $\hat{s}_0$ to the true total intensity s_0. Then, the normalized Stokes vector components are

$$\hat{s}_1/s_0 \sim \mathcal{N}\left(s_1/s_0, \sigma_v^2/s_0^2\right), \;\; \hat{s}_2/s_0 \sim \mathcal{N}\left(s_2/s_0, \sigma_v^2/s_0^2\right). \tag{6}$$

The components of the normalized Stokes vector follow a Gaussian distribution. From the DoLP equation and Equation (6), the DoLP is distributed as a Rician distribution. It is expressed as $\hat{\psi} \sim \text{Rice}\left(\psi, \sigma_v/s_0\right)$. The probability density function (PDF) of DoLP is expressed as

$$\begin{aligned} &f_{\text{Rice}}\left(\hat{\psi}|\psi, \sigma_v/s_0\right) \\ &= \frac{s_0^2\hat{\psi}}{\sigma_v^2}\exp\left(\frac{-s_0^2\left(\hat{\psi}^2 + \psi^2\right)}{2\sigma_v^2}\right) I_0\left(\frac{s_0^2\hat{\psi}\psi}{\sigma_v^2}\right). \end{aligned} \tag{7}$$

The mean of the distribution is represented as

$$\mathrm{E}\left[\hat{\psi}\right] = \frac{\sigma_v}{s_0}\sqrt{\frac{\pi}{2}}L_{1/2}\left(\frac{-s_0^2\psi^2}{2\sigma_v^2}\right). \tag{8}$$

Figures 3(b) and (c) exemplify the distribution of DoLP and its associated bias from the parameters, specifically the DoLP and the ratio of s_0 to Stokes vector noise.

4.4. AoLP noise model

The noise model of AoLP represents the marginal distribution of the phase of $\hat{s}_1$ and $\hat{s}_2$. In Figure 3(a), we observe the line integral along the green line. The PDF of AoLP is expressed as

$$\begin{aligned} &f_\phi\left(2\hat{\phi}|s_1, s_2, \sigma_v^2\right) = \int_0^\infty f\left(\hat{s}_1, \hat{s}_2\right) r dr \\ &= \frac{1}{2\pi}\exp\left(-\frac{s_{pol}^2}{2\sigma_v^2}\right) + \frac{s_{pol}\cos\left(2\hat{\phi} - 2\phi\right)}{\sqrt{2\pi}\sigma_v} \\ &\cdot \exp\left(-\frac{s_{pol}^2\sin^2\left(2\hat{\phi} - 2\phi\right)}{2\sigma_v^2}\right)\Phi\left(\frac{s_{pol}\cos\left(2\hat{\phi} - 2\phi\right)}{\sigma_v}\right), \end{aligned} \tag{9}$$

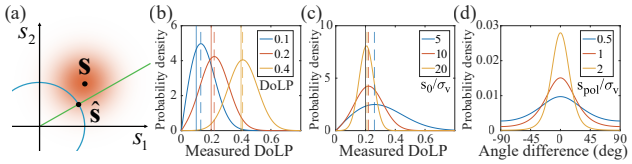

Figure 3. (a) Description of the noise distribution: The noise distribution of a real vector $\mathbf{s}$ is illustrated in red, while the DoLP distribution for an arbitrary observation $\hat{\mathbf{s}}$ is depicted as the line integral of the blue circle. The AoLP distribution corresponds to the integral of the green line. (b) Distribution of observed DoLP in relation to true DoLP: The vertical solid line signifies the true DoLP, and the vertical dashed line indicates the biased maximum. (c) Distribution of observed DoLP concerning the ratio of s_0 and Stokes vector noise: The vertical solid line represents the true DoLP, while the vertical dashed line symbolizes the biased maximum. (d) Distribution of observed AoLP relative to the ratio of s_{pol} and the Stokes vector noise.

where Φ is the cumulative distribution function of the standard normal distribution. The entire integration process is detailed in the supplemental material. The PDF is symmetric about the true AoLP, making the mean unbiased. If the ratio of the polarization intensity to the Stokes vector noise is zero, the distribution becomes a uniform distribution with a density $1/\pi$. If the polarization intensity is much larger than the Stokes vector noise ($s_{pol} \gg \sigma_v$), it can be approximated by a Gaussian distribution. Figure 3(d) illustrates an example of the AoLP distribution based on the ratio of s_{pol} to Stokes vector noise.

5. Noise analysis

5.1. Validation for noise analysis model

We validate the noise analysis model using object scenes in a darkroom. We obtain pseudo true values from the mean of 10,000 burst images. The observed values are the pixel values of each image from the scenes. Our noise distribution model consists of three parts, and we display the distribution of these parts using a histogram. For validation of the Stokes vector noise model, refer to the supplemental.

We obtain the observed distribution of DoLP and AoLP differences using a histogram. The DoLP distribution is a function of the true DoLP and the signal-to-noise ratio of s_0. To validate the model for each parameter, a 3D histogram is required, based on the true DoLP, the SNR of s_0, and the observed DoLP value. The differences between the true AoLP and the observed AoLP are distributed as a function of the SNR of s_{pol}. Similarly to DoLP, we obtain a 2D histogram from the samples.

The results are illustrated in Figure 4. The colored lines represent the observed histogram for each SNR, while the black lines depict our estimated probability density functions. The histograms are normalized by the sample size and the bin width to match the scale of the probability density function. The estimated distribution is not merely the outcome of curve fitting to the observed histogram; it reflects data that closely resembles the observed values. For the same true DoLP, the biases vary with SNR, as estimated in Equation (8).

Table 1. Comparison among the polarized image datasets through noise level estimation. Bold text signifies the result with the least noise in that metric.

Dataset	Mean (std.dev.)$\times 10^3 \downarrow$	PSNR$\uparrow$
KAUST [55]	2.733 (1.383)	50.30
RSP [40]	1.747 (2.231)	50.96
MCubeS [45]	0.973 (0.369)	59.65
Spectro-polarimetric [34]	0.346 (0.252)	67.37
Our dataset	**0.056 (0.076)**	**80.50**

5.2. Comparison with polarization datasets

We compare the noise levels of our GT dataset with those of other polarization image datasets. Our dataset is the first to provide noise statistics for polarization image datasets; thus, prior datasets do not calculate or provide their own noise statistics. We cannot make direct comparisons using noise statistics; therefore, we estimate the noise level from the s_0 images utilizing a single-image noise level estimation method for RGB images [10].

We select general scene polarization RGB image datasets for comparison: the KAUST polarization image dataset [55], the RSP dataset [40], the MCubeS dataset [45], and the spectro-polarimetric dataset [34]. We focus exclusively on real captured, visible spectrum, and RGB images, thus excluding synthetic, near-infrared, or hyperspectral images from these datasets. The results of the noise level estimation are presented in Table 1. Our dataset demonstrates the lowest estimated noise level in both the absolute mean and squared mean, as indicated in PSNR.

5.3. Statistics of our dataset

Using our noise analysis model, we estimate the statistics of the physical values from our static scene dataset. The model treats the pixel values as Gaussian random variables in Equation (3). Additionally, we captured the static scene under static illumination, resulting in independent random variables with the same Gaussian distribution for pixel values over time at the same position. Through the arithmetic of Gaussian random variables, the variance of the mean from N independent Gaussian random variables reduces to 1/N. Similarly, we estimated each pixel's variance as the variance of a single pixel divided by the number of captured frames. From the mean values and estimated variances, DoLP and AoLP distributions can be reconstructed. Consequently, we accumulated the per-pixel statistics from the per-pixel DoLP and AoLP distributions into a histogram. The histogram and its summary are shown in Figure 6 and

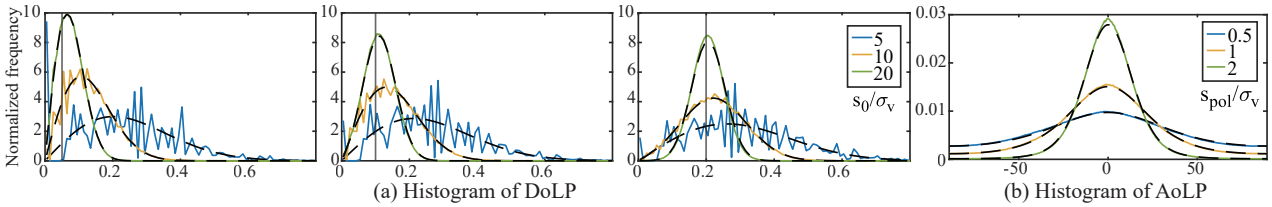

(a) Histogram of DoLP (b) Histogram of AoLP

Figure 4. Histogram of polarization properties. The histogram values are normalized to a probability density scale. The black dashed line indicates the distribution predicted by our model. Each colored line represents the measured DoLP distribution at the corresponding ratio of the Stokes component value to the Stokes vector noise. (a) Histogram of DoLP. Each histogram displays the distribution for true DoLP values of 0.05, 0.1, and 0.2, respectively. The vertical line marks the location of the true DoLP value. (b) Histogram of AoLP.

Table 2. Dataset statistics predicted by the model indicate that the image-like component s_0 is represented as a general image metric, while the polarization characteristics are denoted as the percentage of pixels satisfying the model-based metric. Bold text emphasizes the result with the least noise in that context metric.

	Metric		Single image	Our dataset
s_0	PSNR		52.61	**82.83**
DoLP	Bias	< 0.01	14.64 %	**99.97** %
		< 0.001	1.47 %	**97.85** %
	Std.dev.	< 0.1	64.20 %	**100.00** %
		< 0.01	0.10 %	**97.30** %
AoLP	Std.dev.	$< 10°$	11.57 %	**97.41** %
		$< 5°$	4.83 %	**91.86** %

Table 2.

Although the PSNR of the s_0 from the single captures is reasonable for the image dataset, around 90% of pixels exhibit over a 10-degree standard deviation in the AoLP, and more than 80% of pixels display over a 0.01 bias in the DoLP. Our dataset minimizes noise through static burst captures, ensuring robustness in the polarization property domain, not just the intensity domain.

6. Application

Our datasets make it possible to develop and validate learning-based burst super-resolution of polarization images. Therefore, we validate the neural network models in the polarization image domain. We select 5 state-of-the-art burst SR networks for comparison: MFIR [8], BSRT [47], Burstormer [18], FBANet [69], and BurstM [37]. The models are adopted for RGB images, so we modified the code as needed, such as altering the number of input and output channels, performing demosaicking if required, or using optical flow with s_0. Refer to the supplemental document for the training details. We validate which strategy performs better for burst SR in polarization images by comparing RGB pretrained models with those trained on polarization image datasets. Next, we compare burst SR networks using the PolarBurstSR dataset.

6.1. Comparison with RGB pretrained model

As a validation of the training in the polarization image domain, we compare pre-trained models on RGB images with trained models on the polarization image dataset. The input channels, output channels, and Bayer patterns differ between RGB and polarization images; therefore, the RGB pre-trained model cannot be applied directly. We considered the differences in the Bayer patterns to adapt the RGB pre-trained model for use with polarization raw images. The polarization Bayer pattern for each of the 0°, 45°, 90°, and 135°linear polarization angles can be represented as a CFA Bayer pattern with two pixels dilation. Each angle's linear polarization image follows the super-resolution process like an RGB raw image, and they are aligned by considering their original positions in the polarization Bayer pattern.

The results are presented in Figure 5 and Table 3. The models trained with polarization are designated by the prefix p- in the table. Training on the polarization dataset demonstrates performance improvements across most models and metrics, regardless of whether the dataset is real or synthetic. It produces clearer images for the s_0 components and more stable images in the DoLP images, while RGB pre-trained models yield varying shapes depending on the specific model. The comparison in the AoLP image shows a more significant difference. The low-resolution input fails to generate a normal signal due to noise interference, and the RGB pre-trained model shows some geometric features but lacks sufficient information to reconstruct the geometry. Conversely, the polarization model, like GT, effectively reflects the scene's geometric information. Overall, the results highlight that the contribution of information propagation among each polarization image is more significant than the size of the training dataset.

6.2. Comparison among burst SR models

We compare the burst SR models in the PolarBurstSR dataset. The results are presented in Figure 5 and Table 3. BSRT achieves the best result for the metric s_0, which closely resembles the RGB image. However, it does not perform best in terms of polarization characteristics, DoLP, and AoLP. FBANet excels in the polarization characteristics, ranking second or third in s_0. Nevertheless, in the qual-

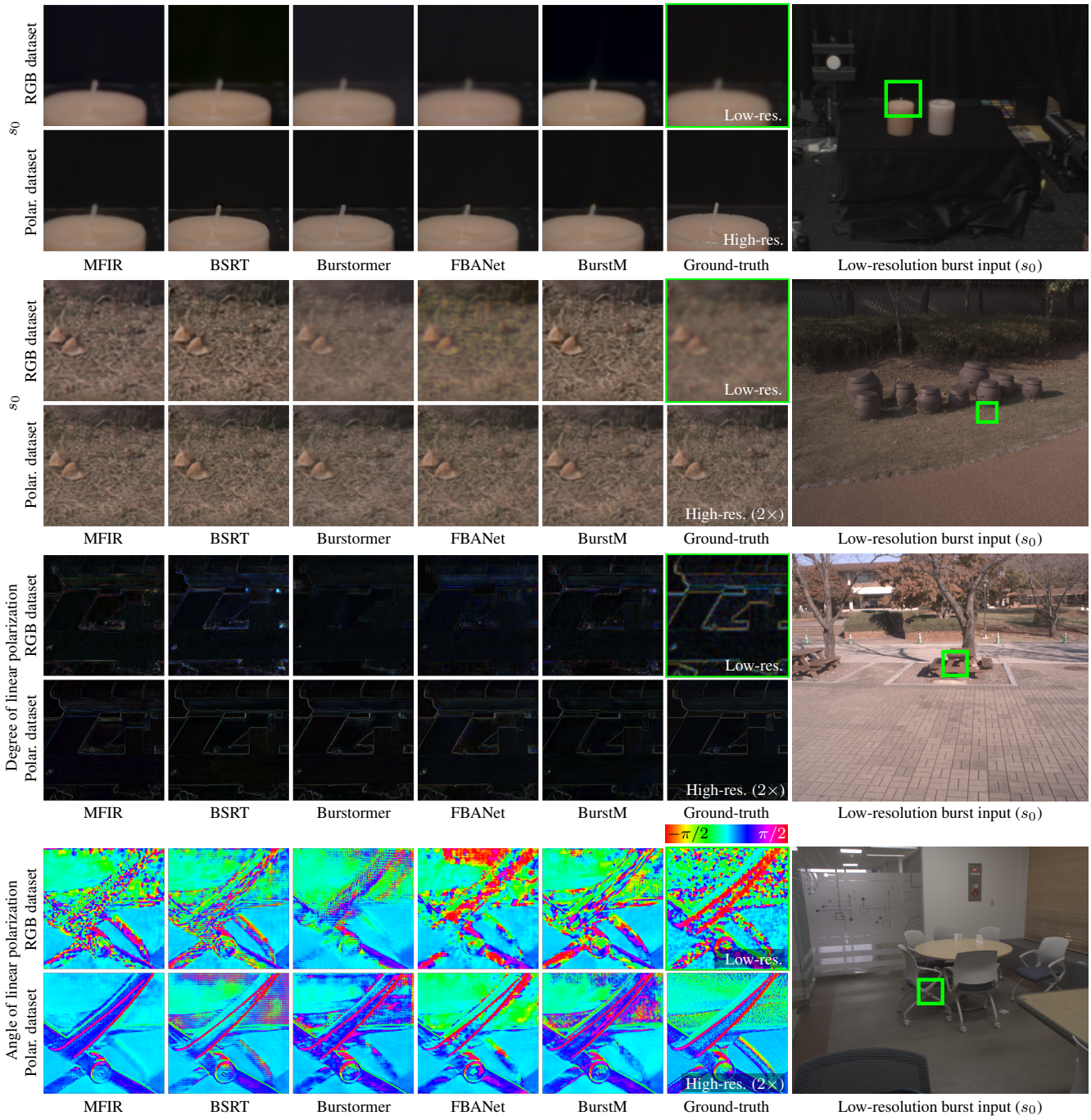

Figure 5. Qualitative comparisons of 2× burst super-resolution results on the PolarNS dataset with various scene conditions. Overall, the trained models in the polarization dataset in the lower row are sharper than those in the RGB dataset in the upper row and show results closer to GT. In particular, in AoLP, although much geometric information is lost due to noise in the LR and RGB-trained models, this information is reconstructed in the polarization-trained models.

itative comparison, the advantage in the polarization characteristics is not clearly demonstrated, while the s_0 results show BSRT's clarity. This may be due to the absence of a metric to assess the significance of DoLP or AoLP results, as PSNR, a metric reliant on mean squared error, is employed.

7. Discussion

While our model, datasets, and analysis aim to produce accurate results, several limitations remain, leaving these topics open for future research. We discuss limitations in noise analysis across datasets, the shot-and-read noise model un-

Table 3. Quantitative evaluation. Green text indicates improvement, while red text denotes a performance decrease. We also mark the top score as **bold text**. The prefix *p-* indicates that it is trained on a polarization dataset. In most metrics, models trained on polarization datasets perform significantly better.

Method	Synthetic polar dataset					Real polar dataset				
	s_0 PSNR↑	s_0 SSIM↑	s_0 LPIPS↓	DoLP PSNR↑	AoLP PSNR↑	s_0 PSNR↑	s_0 SSIM↑	s_0 LPIPS↓	DoLP PSNR↑	AoLP PSNR↑
MFIR [8]	32.28	0.870	0.091	16.79	14.90	43.16	0.962	0.084	23.76	16.67
p-MFIR	42.18 +9.90	0.971 +0.101	0.035 -0.056	21.26 +4.47	15.97 +1.07	45.18 +2.02	0.977 +0.015	0.063 -0.021	22.00 -1.76	15.74 -0.93
BSRT [47]	31.95	0.860	0.067	20.70	14.29	44.15	0.973	0.073	23.03	16.14
p-BSRT	**43.75** +11.80	**0.979** +0.119	**0.021** -0.046	20.31 -0.39	**17.09** +2.80	**45.69** +1.54	**0.979** +0.006	**0.051** -0.022	25.17 +2.14	17.06 +0.92
Burstormer [18]	32.03	0.862	0.071	21.36	15.16	40.72	0.938	0.147	24.90	16.95
p-Burstormer	41.12 +9.09	0.965 +0.103	0.049 -0.022	**24.49** +3.13	16.79 +1.63	43.29 +2.57	0.973 +0.035	0.061 -0.086	25.84 +0.94	17.36 +0.41
FBAnet [69]	33.94	0.892	0.201	15.29	13.20	40.57	0.946	0.138	24.28	16.14
p-FBAnet	36.08 +2.14	0.914 +0.018	0.193 -0.008	21.23 +5.94	16.88 +3.68	45.64 +5.07	0.976 +0.030	0.055 -0.083	**26.92** +2.64	**18.14** +2.00
BurstM [37]	32.00	0.860	0.067	21.77	15.37	43.82	0.972	0.075	22.78	16.64
p-BurstM	39.42 +7.42	0.953 +0.093	0.063 -0.004	21.34 -0.43	16.08 +0.71	45.19 +1.37	0.975 +0.003	0.063 -0.012	23.67 +0.89	16.32 -0.32

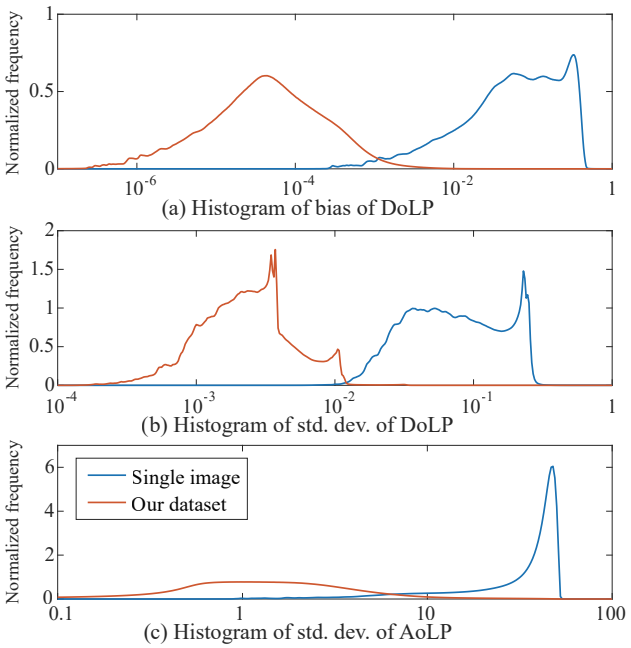

Figure 6. Histogram of the estimated DoLP bias, the DoLP standard deviation, and the AoLP standard deviation for the dataset. The histogram is computed in bins on a logarithmic scale, and the values are normalized to a probability density scale.

derlying noise analysis, scene variety due to the inability to capture dynamic objects and illumination, and differences between burst images and GT images due to camera locations. Please refer to the supplemental material for additional information.

8. Conclusion

We introduce PolarNS and PolarBurstSR, two novel datasets designed to enhance noise analysis and burst super-resolution in polarization imaging. PolarNS offers a detailed characterization of polarization noise statistics, enabling precise modeling and evaluation of noise propagation. Our polarization noise analysis model further quantifies noise behavior, providing a rigorous framework for assessing the confidence of polarization-derived properties. As an application, we demonstrate the effectiveness of burst super-resolution for polarization imaging by comparing models trained on conventional RGB datasets with those trained on our dedicated polarization dataset. The results underscore the importance of polarization-specific training in improving both intensity image resolution and the accuracy of polarization properties. By publicly releasing our datasets, pretrained models, and training pipelines, we aim to establish a benchmark for polarization burst super-resolution and promote future research in the denoising and high-resolution reconstruction of polarization images.

Acknowledgements

Min H. Kim acknowledges the Samsung Research Funding & Incubation Center (SRFC-IT2402-02), the Korea NRF grant (RS-2024-00357548), the MSIT/IITP of Korea (RS-2022-00155620, RS-2024-00398830, 2022-0-00058, and 2017-0-00072), Microsoft Research Asia, and Samsung Electronics.

References

[1] Gary Atkinson and E.R. Hancock. Recovery of surface orientation from diffuse polarization. *IEEE Transactions on Image Processing*, 15(6):1653–1664, 2006. 1, 2

[2] Dejan Azinovic, Olivier Maury, Christophe Hery, Matthias Niessner, and Justus Thies. High-res facial appearance capture from polarized smartphone images. In *Proceedings of the IEEE/CVF Conference on Computer Vision and Pattern Recognition (CVPR)*, 2023. 1

[3] Yunhao Ba, Alex Gilbert, Franklin Wang, Jinfa Yang, Rui Chen, Yiqin Wang, Lei Yan, Boxin Shi, and Achuta Kadambi. Deep shape from polarization. In *Computer Vision – ECCV 2020*, pages 554–571, Cham, 2020. Springer International Publishing. 1, 2

[4] Seung-Hwan Baek and Felix Heide. Polarimetric spatio-temporal light transport probing. *ACM Transactions on Graphics (Proc. SIGGRAPH Asia)*, 40(6), 2021. 1, 2

[5] Seung-Hwan Baek and Felix Heide. All-photon polarimetric time-of-flight imaging. *Proceedings of the IEEE Conference on Computer Vision and Pattern Recognition (CVPR)*, 2022. 1, 2

[6] Chuanbiao Bai, Zhaoxiang Jiang, Jiangcheng Zhao, Shangquan Wu, and Qingchuan Zhang. Noise analysis in stokes parameter reconstruction for division-of-focal-plane polarimeters. *Appl. Opt.*, 61(24):7084–7094, 2022. 2

[7] Goutam Bhat, Martin Danelljan, Luc Van Gool, and Radu Timofte. Deep burst super-resolution. In *Proceedings of the IEEE/CVF conference on computer vision and pattern recognition*, pages 9209–9218, 2021. 2, 3

[8] Goutam Bhat, Martin Danelljan, Fisher Yu, Luc Van Gool, and Radu Timofte. Deep reparametrization of multi-frame super-resolution and denoising. In *Proceedings of the IEEE/CVF International Conference on Computer Vision (ICCV)*, pages 2460–2470, 2021. 3, 6, 8

[9] Goutam Bhat, Michaël Gharbi, Jiawen Chen, Luc Van Gool, and Zhihao Xia. Self-supervised burst super-resolution. In *2023 IEEE/CVF International Conference on Computer Vision (ICCV)*, pages 10571–10580, 2023. 3

[10] Guangyong Chen, Fengyuan Zhu, and Pheng Ann Heng. An efficient statistical method for image noise level estimation. In *2015 IEEE International Conference on Computer Vision (ICCV)*, pages 477–485, 2015. 5

[11] Yingkai Chen, Zhongmin Zhu, Zuodong Liang, Leanne E. Iannucci, Spencer P. Lake, and Viktor Gruev. Analysis of signal-to-noise ratio of angle of polarization and degree of polarization. *OSA Continuum*, 4(5):1461–1472, 2021. 2

[12] Zhaopeng Cui, Jinwei Gu, Boxin Shi, Ping Tan, and Jan Kautz. Polarimetric multi-view stereo. In *Proceedings of the IEEE Conference on Computer Vision and Pattern Recognition*, pages 1558–1567, 2017. 1

[13] Zhaopeng Cui, Viktor Larsson, and Marc Pollefeys. Polarimetric relative pose estimation. *Proceedings of the IEEE International Conference on Computer Vision*, 2019-October: 2671–2680, 2019. 1

[14] Jun Dai, François Goudail, Matthieu Boffety, and Jun Gao. Estimation precision of full polarimetric parameters in the presence of additive and poisson noise. *Opt. Express*, 26 (26):34081–34093, 2018. 2

[15] Akshat Dave, Yongyi Zhao, and Ashok Veeraraghavan. Pandora: Polarization-aided neural decomposition of radiance. In *Computer Vision – ECCV 2022*, pages 538–556, Cham, 2022. Springer Nature Switzerland. 1, 2

[16] Valentin Deschaintre, Yiming Lin, and Abhijeet Ghosh. Deep polarization imaging for 3d shape and svbrdf acquisition. In *Proceedings of the IEEE/CVF Conference on Computer Vision and Pattern Recognition (CVPR)*, 2021.

[17] Yuqi Ding, Yu Ji, Mingyuan Zhou, Sing Bing Kang, and Jinwei Ye. Polarimetric helmholtz stereopsis. In *2021 IEEE/CVF International Conference on Computer Vision (ICCV)*, pages 5017–5026, 2021. 1

[18] Akshay Dudhane, Syed Waqas Zamir, Salman Khan, Fahad Shahbaz Khan, and Ming-Hsuan Yang. Burstormer: Burst image restoration and enhancement transformer. In *Proceedings of the IEEE/CVF Conference on Computer Vision and Pattern Recognition (CVPR)*, pages 5703–5712, 2023. 3, 6, 8

[19] M. Elad and A. Feuer. Restoration of a single superresolution image from several blurred, noisy, and undersampled measured images. *IEEE Transactions on Image Processing*, 6(12):1646–1658, 1997. 2

[20] Shuai Fang, XiuShan Xia, Xing Huo, and ChangWen Chen. Image dehazing using polarization effects of objects and airlight. *Opt. Express*, 22(16):19523–19537, 2014. 1, 2

[21] Sina Farsiu, Michael Elad, and Peyman Milanfar. Multiframe demosaicing and super-resolution from undersampled color images. In *Computational Imaging II*, pages 222 – 233. International Society for Optics and Photonics, SPIE, 2004. 2

[22] Yoshiki Fukao, Ryo Kawahara, Shohei Nobuhara, and Ko Nishino. Polarimetric normal stereo. In *2021 IEEE/CVF Conference on Computer Vision and Pattern Recognition (CVPR)*, pages 682–690, 2021. 1

[23] Victor L. Gamiz and John F. Belsher. Performance limitations of a four-channel polarimeter in the presence of detection noise. In *Polarization: Measurement, Analysis, and Remote Sensing II*, pages 204 – 216. International Society for Optics and Photonics, SPIE, 1999. 2

[24] Abhijeet Ghosh, Tongbo Chen, Pieter Peers, Cyrus A. Wilson, and Paul Debevec. Circularly polarized spherical illumination reflectometry. *ACM Trans. Graph.*, 29(6), 2010. 1

[25] Abhijeet Ghosh, Graham Fyffe, Borom Tunwattanapong, Jay Busch, Xueming Yu, and Paul Debevec. Multiview face capture using polarized spherical gradient illumination. *ACM Trans. Graph.*, 30(6):1–10, 2011. 1

[26] Dennis H. Goldstein and Russell A. Chipman. Error analysis of a mueller matrix polarimeter. *J. Opt. Soc. Am. A*, 7(4): 693–700, 1990. 2

[27] Paulo Gotardo, Jérémy Riviere, Derek Bradley, Abhijeet Ghosh, and Thabo Beeler. Practical dynamic facial appearance modeling and acquisition. *ACM Trans. Graph.*, 37(6), 2018. 1

[28] François Goudail. Noise minimization and equalization for stokes polarimeters in the presence of signal-dependent poisson shot noise. *Opt. Lett.*, 34(5):647–649, 2009. 2

[29] François Goudail and Arnaud Bénière. Estimation precision of the degree of linear polarization and of the angle of polarization in the presence of different sources of noise. *Appl. Opt.*, 49(4):683–693, 2010. 2

[30] Hyunho Ha, Inseung Hwang, Nestor Monzon, Jaemin Cho, Donggun Kim, Seung-Hwan Baek, Adolfo Muñoz, Diego Gutierrez, and Min H. Kim. Polarimetric bssrdf acquisition of dynamic faces. *ACM Transactions on Graphics (Proc. SIGGRAPH Asia 2024)*, 43(6), 2024. 1

[31] Cong Phuoc Huynh, Antonio Robles-Kelly, and Edwin R. Hancock. Shape and refractive index from single-view spectro-polarimetric images. *Int. J. Comput. Vision*, 101(1): 64–94, 2013. 1, 2

[32] Michal Irani and Shmuel Peleg. Improving resolution by image registration. *CVGIP: Graphical Models and Image Processing*, 53(3):231–239, 1991. 2

[33] Daniel S. Jeon, Andreas Meuleman, Seung-Hwan Baek, and Min H. Kim. Polarimetric itof: Measuring high-fidelity depth through scattering media. In *IEEE Conference on Computer Vision and Pattern Recognition (CVPR)*, 2023. 1, 2

[34] Yujin Jeon, Eunsue Choi, Youngchan Kim, Yunseong Moon, Khalid Omer, Felix Heide, and Seung-Hwan Baek. Spectral and polarization vision: Spectro-polarimetric real-world dataset. In *Proceedings of the IEEE/CVF Conference on Computer Vision and Pattern Recognition (CVPR)*, pages 22098–22108, 2024. 2, 5

[35] Achuta Kadambi, Vage Taamazyan, Boxin Shi, and Ramesh Raskar. Polarized 3d: High-quality depth sensing with polarization cues. In *Proc. ICCV*, pages 3370–3378. IEEE Computer Society, 2015. 1

[36] Agastya Kalra, Vage Taamazyan, Supreeth Krishna Rao, Kartik Venkataraman, Ramesh Raskar, and Achuta Kadambi. Deep polarization cues for transparent object segmentation. In *2020 IEEE/CVF Conference on Computer Vision and Pattern Recognition (CVPR)*, pages 8599–8608, 2020. 1, 2

[37] EungGu Kang, Byeonghun Lee, Sunghoon Im, and Kyong Hwan Jin. Burstm: Deep burst multi-scale sr using fourier space with optical flow. In *Computer Vision – ECCV 2024: 18th European Conference, Milan, Italy, September 29–October 4, 2024, Proceedings, Part XLII*, page 459–477, Berlin, Heidelberg, 2024. Springer-Verlag. 3, 6, 8

[38] Naejin Kong, Yu-Wing Tai, and Joseph S. Shin. A physically-based approach to reflection separation: From physical modeling to constrained optimization. *IEEE Transactions on Pattern Analysis and Machine Intelligence*, 36(2): 209–221, 2014. 1, 2

[39] Meredith Kupinski, Russell Chipman, and Eric Clarkson. Relating the statistics of the angle of linear polarization to measurement uncertainty of the Stokes vector. *Optical Engineering*, 53(11):113108, 2014. 2

[40] Teppei Kurita, Yuhi Kondo, Legong Sun, and Yusuke Moriuchi. Simultaneous acquisition of high quality rgb image and polarization. In *Proceedings of the IEEE/CVF Winter Conference on Applications of Computer Vision (WACV)*, pages 178–188, 2023. 2, 5

[41] Chenyang Lei, Xuhua Huang, Mengdi Zhang, Qiong Yan, Wenxiu Sun, and Qifeng Chen. Polarized reflection removal with perfect alignment in the wild. In *IEEE/CVF Conference on Computer Vision and Pattern Recognition (CVPR)*, 2020. 1, 2

[42] Chenyang Lei, Chenyang Qi, Jiaxin Xie, Na Fan, Vladlen Koltun, and Qifeng Chen. Shape from Polarization for Complex Scenes in the Wild . In *2022 IEEE/CVF Conference on Computer Vision and Pattern Recognition (CVPR)*, pages 12622–12631, Los Alamitos, CA, USA, 2022. IEEE Computer Society. 1, 2

[43] Chenhao Li, Taishi Ono, Takeshi Uemori, Hajime Mihara, Alexander Gatto, Hajime Nagahara, and Yusuke Moriuchi. Neisf: Neural incident stokes field for geometry and material estimation. In *Proceedings of the IEEE/CVF Conference on Computer Vision and Pattern Recognition (CVPR)*, pages 21434–21445, 2024. 1

[44] Xiaobo Li, Haofeng Hu, François Goudail, and Tiegen Liu. Fundamental precision limits of full stokes polarimeters based on dofp polarization cameras for an arbitrary number of acquisitions. *Opt. Express*, 27(22):31261–31272, 2019. 2

[45] Yupeng Liang, Ryosuke Wakaki, Shohei Nobuhara, and Ko Nishino. Multimodal material segmentation. In *2022 IEEE/CVF Conference on Computer Vision and Pattern Recognition (CVPR)*, pages 19768–19776, 2022. 2, 5

[46] Fei Liu, Lei Cao, Xiaopeng Shao, Pingli Han, and Xiangli Bin. Polarimetric dehazing utilizing spatial frequency segregation of images. *Appl. Opt.*, 54(27):8116–8122, 2015. 1, 2

[47] Ziwei Luo, Youwei Li, Shen Cheng, Lei Yu, Qi Wu, Zhihong Wen, Haoqiang Fan, Jian Sun, and Shuaicheng Liu. Bsrt: Improving burst super-resolution with swin transformer and flow-guided deformable alignment. In *Proceedings of the IEEE/CVF Conference on Computer Vision and Pattern Recognition*, pages 998–1008, 2022. 1, 3, 6, 8

[48] Youwei Lyu, Zhaopeng Cui, Si Li, Marc Pollefeys, and Boxin Shi. Reflection separation using a pair of unpolarized and polarized images. In *Advances in Neural Information Processing Systems 32 (NeurIPS)*, pages 14559–14569. Curran Associates, Inc., 2019. 1, 2

[49] Wan-Chun Ma, Tim Hawkins, Pieter Peers, Charles-Felix Chabert, Malte Weiss, and Paul Debevec. Rapid acquisition of specular and diffuse normal maps from polarized spherical gradient illumination. In *Proceedings of the 18th Eurographics Conference on Rendering Techniques*, page 183–194, Goslar, DEU, 2007. Eurographics Association. 1

[50] Haiyang Mei, Bo Dong, Wen Dong, Jiaxi Yang, Seung-Hwan Baek, Felix Heide, Pieter Peers, Xiaopeng Wei, and Xin Yang. Glass segmentation using intensity and spectral polarization cues. In *2022 IEEE/CVF Conference on Computer Vision and Pattern Recognition (CVPR)*, pages 12612–12621, 2022. 1, 2

[51] Miyazaki, Tan, Hara, and Ikeuchi. Polarization-based inverse rendering from a single view. In *Proceedings Ninth IEEE*

International Conference on Computer Vision, pages 982–987 vol.2, 2003. 1, 2

[52] Robert Perkins and Viktor Gruev. Signal-to-noise analysis of stokes parameters in division of focal plane polarimeters. *Opt. Express*, 18(25):25815–25824, 2010. 2

[53] S. Plaszczynski, L. Montier, F. Levrier, and M. Tristram. A novel estimator of the polarization amplitude from normally distributed Stokes parameters. *Monthly Notices of the Royal Astronomical Society*, 439(4):4048–4056, 2014. 2

[54] Yu Qiao, Bo Dong, Ao Jin, Yu Fu, Seung-Hwan Baek, Felix Heide, Pieter Peers, Xiaopeng Wei, and Xin Yang. Multi-view spectral polarization propagation for video glass segmentation. In *Proceedings of the International Conference on Computer Vision (ICCV)*, 2023. 1, 2

[55] Simeng Qiu, Qiang Fu, Congli Wang, and Wolfgang Heidrich. Linear polarization demosaicking for monochrome and colour polarization focal plane arrays. *Computer Graphics Forum*, 40(6):77–89, 2021. 2, 5

[56] Jason Lee Quinn. Bayesian analysis of polarization measurements. *Astronomy & Astrophysics*, 538:A65, 2012. 2, 4

[57] Jérémy Riviere, Ilya Reshetouski, Luka Filipi, and Abhijeet Ghosh. Polarization imaging reflectometry in the wild. *ACM Trans. Graph.*, 36(6), 2017. 1

[58] Jérémy Riviere, Paulo Gotardo, Derek Bradley, Abhijeet Ghosh, and Thabo Beeler. Single-shot high-quality facial geometry and skin appearance capture. *ACM Trans. Graph.*, 39(4), 2020. 1

[59] Stéphane Roussel, Matthieu Boffety, and François Goudail. Polarimetric precision of micropolarizer grid-based camera in the presence of additive and poisson shot noise. *Opt. Express*, 26(23):29968–29982, 2018. 2

[60] D. S. Sabatke, M. R. Descour, E. L. Dereniak, W. C. Sweatt, S. A. Kemme, and G. S. Phipps. Optimization of retardance for a complete stokes polarimeter. *Opt. Lett.*, 25(11):802–804, 2000. 2

[61] Y.Y. Schechner, S.G. Narasimhan, and S.K. Nayar. Instant dehazing of images using polarization. In *Proc. IEEE Conference on Computer Vision and Pattern Recognition. CVPR 2001*, pages I–I, 2001. 1, 2

[62] Dominik Scheuble, Chenyang Lei, Seung-Hwan Baek, Mario Bijelic, and Felix Heide. Polarization wavefront lidar: Learning large scene reconstruction from polarized wavefronts. In *Proceedings of the IEEE/CVF Conference on Computer Vision and Pattern Recognition*, pages 21241–21250, 2024. 1, 2

[63] JFL Simmons and BG Stewart. Point and interval estimation of the true unbiased degree of linear polarization in the presence of low signal-to-noise ratios. *Astronomy and Astrophysics (ISSN 0004-6361), vol. 142, no. 1, Jan. 1985, p. 100-106. Research supported by the Science and Engineering Research Council.*, 142:100–106, 1985. 2, 4

[64] William A. P. Smith, Ravi Ramamoorthi, and Silvia Tozza. Linear depth estimation from an uncalibrated, monocular polarisation image. In *Computer Vision – ECCV 2016*, pages 109–125, Cham, 2016. Springer International Publishing. 1

[65] Yoshitate Takakura and Jawad Elsayed Ahmad. Noise distribution of mueller matrices retrieved with active rotating polarimeters. *Appl. Opt.*, 46(30):7354–7364, 2007. 2

[66] Chaoran Tian, Weihong Pan, Zimo Wang, Mao Mao, Guofeng Zhang, Hujun Bao, Ping Tan, and Zhaopeng Cui. Dps-net: Deep polarimetric stereo depth estimation. In *Proceedings of the IEEE/CVF International Conference on Computer Vision*, pages 3569–3579, 2023. 2

[67] Silvia Tozza, William A.P. Smith, Dizhong Zhu, Ravi Ramamoorthi, and Edwin R. Hancock. Linear Differential Constraints for Photo-Polarimetric Height Estimation. *Proceedings of the IEEE International Conference on Computer Vision*, 2017-October:2298–2306, 2017. 1

[68] R. Y. Tsai and T. S. Huang. Multiframe image restoration and registration. *Advances in Computer Vision and Image Processing*, 1:317–339, 1984. 2

[69] Pengxu Wei, Yujing Sun, Xingbei Guo, Chang Liu, Guanbin Li, Jie Chen, Xiangyang Ji, and Liang Lin. Towards real-world burst image super-resolution: Benchmark and method. In *Proceedings of the IEEE/CVF International Conference on Computer Vision (ICCV)*, pages 13233–13242, 2023. 3, 6, 8

[70] Patrick Wieschollek, Orazio Gallo, Jinwei Gu, and Jan Kautz. Separating reflection and transmission images in the wild. In *European Conference on Computer Vision (ECCV)*, 2018. 1, 2

[71] Bartlomiej Wronski, Ignacio Garcia-Dorado, Manfred Ernst, Damien Kelly, Michael Krainin, Chia-Kai Liang, Marc Levoy, and Peyman Milanfar. Handheld multi-frame super-resolution. *ACM Trans. Graph.*, 38(4), 2019. 2

[72] Han Yufei, Guo Heng, Fukai Koki, Santo Hiroaki, Shi Boxin, Okura Fumio, Ma Zhanyu, and Jia Yunpeng. Nersp: Neural 3d reconstruction for reflective objects with sparse polarized images. In *CVPR*, 2024. 1

[73] Jinyu Zhao, Yusuke Monno, and Masatoshi Okutomi. Polarimetric multi-view inverse rendering. In *Computer Vision – ECCV 2020*, pages 85–102, Cham, 2020. Springer International Publishing. 1

[74] Chu Zhou, Minggui Teng, Yufei Han, Chao Xu, and Boxin Shi. Learning to dehaze with polarization. In *Advances in Neural Information Processing Systems*, pages 11487–11500. Curran Associates, Inc., 2021. 1, 2

[75] Dizhong Zhu and William AP Smith. Depth from a polarisation + rgb stereo pair. In *Proceedings of the IEEE/CVF Conference on Computer Vision and Pattern Recognition (CVPR)*, 2019. 1